Instabilities, motion and deformation of active fluid droplets

Carl A. Whitfield* and Rhoda J. Hawkins Department of Physics and Astronomy, University of Sheffield, Sheffield, UK, S3 7RH (Dated: July 12, 2022)

We consider two minimal models of active fluid droplets that exhibit complex dynamics including steady motion, deformation, rotation and oscillating motion. First we consider a droplet with a concentration of active contractile matter adsorbed to its boundary. We analytically predict activity driven instabilities in the concentration profile, and compare them to the dynamics we find from simulations. Secondly, we consider a droplet of active polar fluid of constant concentration. In this system we predict, motion and deformation of the droplets in certain activity ranges due to instabilities in the polarisation field. Both these systems show spontaneous transitions to motility and deformation which resemble dynamics of the cell cytoskeleton in animal cells.

INTRODUCTION

In animal cells, motility and morphology are strongly coupled and are largely due to the activity of the cell cytoskeleton. Research into these areas is broad and has many applications, from studying metastatic cancer cells to wound healing. In order to mimic aspects of these systems we model, both analytically and numerically, examples of active cytoskeletal material confined to droplets. An active material is defined as driven out-of-equilibrium by the internal energy of its constituent particles [1]. We use the hydrodynamic model of an active polar fluid outlined in [2–4] to model the behaviour of such a material at long length and time scales.

Over the past decade there have been a number of calculations of instabilities and non-equilibrium steady states in active liquid crystals; thin or 2D flat films [2, 5–9], thin cortical layers [10–13], confined in emulsion droplets or vesicles [14–19], and simplified models of animal and plant cells [20–23]. In this paper we model deforming active droplets immersed in a passive fluid using linear perturbation theory. By making justified assumptions, we are able to predict non-equilibrium phase transitions in both of the systems we consider, and predict how the droplet deformation couples to these. We compare these predictions to 2-dimensional simulations [24] which predict the steady state behaviour of the system. Our predictions remain qualitatively similar in 2D and concur with the simulation results.

The models presented here are relevant to active systems in vitro (constructed using techniques in [25-27]) as well mimicking aspects of cell dynamics. The two cases we consider correspond to two limits of active cytoskeletal behaviour (see figure 1) that represent the minimum degrees of freedom required to observe interesting out-of-equilibrium dynamics. In both cases we consider a 1-component model used originally in [2], which allows us to investigate the coupling with droplet shape dynamics analytically.

Firstly, we consider an isotropic layer of contractile active material confined to an interface between two fluids, which has physical similarities to the actomyosin cortex

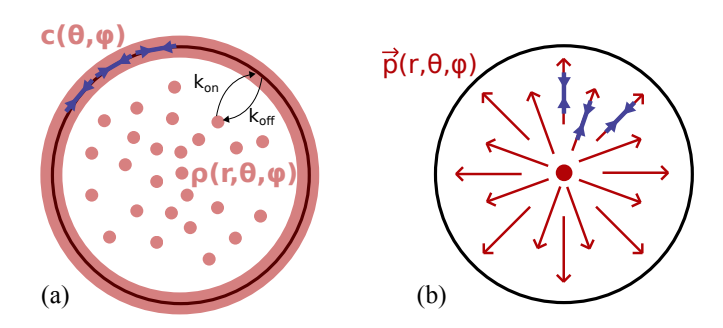


FIG. 1. 2D schematic of (a) Active fluid interface: active concentration c on the droplet interface coupled to the internal concentration ρ . (b) Active polar droplet: constant density of active filaments with local average polarisation \boldsymbol{p} (red arrows). Blue arrows indicate active contractile force dipoles.

in cells. The stresses generated are confined to the plane of the interface giving rise to flows in the surrounding fluid and deformation of the interface itself. Interestingly, diffusion of the active particles through the bulk can result in the formation of multiple peaks becoming the lowest energy unstable mode. Furthermore, simulations show that advection through the bulk can stabilise such modes. This suggests that droplets with an active interface could spontaneously deform and possibly divide due to the feedback from the fluid flow.

Secondly, we consider a highly ordered active polar liquid crystal confined inside a fluid droplet. In this case the polarisation gradients direct the internal stresses giving rise to fluid flow. A polar anchoring condition at the interface means that the deformation of the droplet and polarisation field are strongly coupled. We find in this case there is a separation of swimming and stationary deforming modes, such that extensile activity destabilises the defect position and results in a swimming drop, whereas a contractile activity stabilises the centred defect position and gives rise to deformations of the interface.

MODEL

Active Fluid Interface Model

We consider a fluid droplet described by an interfacial surface Σ separating the contained fluid domain Ω_0 and external fluid domain Ω_1 with viscosities η_0 and η_1 respectively. We define a concentration of active matter $c(\theta, \phi, t)$ on the interface Σ , which alters the droplet surface tension γ such that $\gamma = \gamma_0 - \zeta_c c - Bc^2/2$. γ_0 is the bare surface tension, ζ_c is the activity ($\zeta_c < 0$ for contractile) and B is a passive repulsion force. This higher order repulsive term represents passive pressure, similar to that in [12], which parametrises the compressibility of the active fluid on the interface. Defining the effective activity $\tilde{\zeta} = \zeta_c + Bc_0$ where c_0 is the stationary state concentration, the interface is contractile for $\tilde{\zeta} < 0$.

The force density on the droplet interface is then: $\mathbf{F} = \kappa \gamma \hat{\mathbf{n}} + (\nabla_s \gamma) \hat{\mathbf{t}}_i$, where $\hat{\mathbf{n}} = \hat{\mathbf{n}}(\theta, \phi, t)$ is the outward surface normal, $\hat{t}_i = \hat{t}_i(\theta, \phi, t)$ are the orthogonal surface tangent vectors, $\kappa = \nabla \cdot \hat{\boldsymbol{n}}$ is the local curvature, and $\nabla_s = (\hat{t}_i \cdot \nabla)$ is the surface gradient. The only forces acting on the system originate at the droplet surface Σ , with position $\mathbf{R} = R(\theta, \phi, t)\hat{\mathbf{e}}_r$ assuming this is monotonic with respect to the angular coordinates (θ,ϕ) . Thus, the resulting force density in the fluid is $\mathbf{f}^{\text{ext}}(r,\theta,\phi,t) = \mathbf{F}\delta[r - R(\theta,\phi,t)].$ We ignore inertia taking the low Reynolds' number limit, Re = 0, thus the incompressible fluid flow $(\nabla \cdot \boldsymbol{v} = 0)$ is described by Stokes' equation $\eta_n \nabla^2 v + f^{\text{ext}} - \nabla P = 0$, where $\boldsymbol{v} = \boldsymbol{v}(r, \theta, \phi, t)$ is the fluid velocity, $\boldsymbol{f}^{\text{ext}} = \boldsymbol{f}^{\text{ext}}(r, \theta, \phi, t)$ denotes any external force densities and $P = P(r, \theta, \phi, t)$ is the hydrostatic pressure. We take the limit of a zerothickness interface and assume flow and stress continuity between the two fluids Ω_0 and Ω_1 . This means the active particles act as an active surfactant, rather than a thin viscous layer (as in [8, 11–13]), which allows us to study deformation in a 3D viscous environment.

The evolution of the surface concentration c with respect to time t is:

$$\dot{c} = -\nabla_s \cdot (c\mathbf{V}) + D\nabla_s^2 c - k_{\text{off}} c + k_{\text{on}} \rho_b \,, \tag{1}$$

where $\dot{c} = \partial c/\partial t$, $V = V(\theta, \phi, t) = v(R, \theta, \phi, t)$ is the interface flow velocity, D is the diffusion constant for the active particles on Σ , and $k_{\rm on,off}$ are binding and unbinding rates of the particles with an internal concentration $\rho = \rho(r, \theta, \phi, t)$ such that $\rho_b = \rho_b(\theta, \phi, t) = \rho(R, \theta, \phi, t)$. Note that $k_{\rm on}$ has units of velocity, as it contains the adsorption depth parameter. We assume that the active particles are insoluble in the external fluid, and so the evolution of the bulk concentration ρ is given by:

$$\dot{\rho} = -(\boldsymbol{v} \cdot \nabla)\rho + D_b \nabla^2 \rho \tag{2}$$

with the boundary condition $D_b(\mathbf{n} \cdot \nabla)\rho = k_{\rm on}\rho - k_{\rm off}c$ at r = R, to ensure conservation of mass. The parameter

 D_b is the bulk diffusion constant of the active particles. Here we assume that the active particles only generate stresses at the interface, so the bulk concentration acts as a buffer to recycle the surface concentration.

Active Polar Fluid Drop Model

We utilise the model of an active polar fluid developed by Kruse et al. in [2–4] which has similarities to other continuum models of the cytoskeleton on surfaces (such as [28, 29]). We consider the case where the active fluid has strong local ordering and is far from the isotropic phase so that $|\mathbf{p}|=1$. In the Re=0 limit the total stress in the active polar fluid, $\sigma_{ij}^{\text{tot}}=\sigma_{ij}^{\text{visc}}+\sigma_{ij}^{\text{dist}}+\sigma_{ij}^{\text{act}}$, has viscous, distortion and active contributions respectively where:

$$\begin{split} &\sigma_{ij}^{\mathrm{visc}} = 2\eta_{0,1}u_{ij} = \eta_{0,1}\left(\partial_i v_j + \partial_j v_i\right)\,,\\ &\sigma_{ij}^{\mathrm{dist}} = \frac{\nu}{2}\left(p_i h_j + p_j h_i\right) + \frac{1}{2}\left(p_i h_j - p_j h_i\right) + \sigma_{ij}^{\mathrm{e}}\,,\\ &\sigma_{ij}^{\mathrm{act}} = -\zeta p_i p_j\,. \end{split}$$

The viscous stress is the response to flow assuming a Newtonian fluid. The distortion stress is that of a passive polar liquid crystal due to deviations in filament alignment, where the perpendicular part of the molecular field $h_i = -\delta F/\delta \boldsymbol{p}_j (\delta_{ij} - p_i p_j)$ acts to minimise the free energy functional $F = \int_{\Omega+\Sigma} \mathrm{d}^3 r f$ with respect to \boldsymbol{p} . The Ericksen stress, $\sigma^{\mathrm{e}}_{ij} = f \delta_{ij} - (\partial f/(\partial (\partial_j p_k))) \partial_i p_k$, is a generalisation of the hydrostatic pressure for complex fluids. Finally, the active stress represents the active dipolar force and thus is second order in \boldsymbol{p} .

The free energy functional F gives the equilibrium properties of the system. Here for simplicity we use the one constant approximation of the Frank free energy:

$$F = \int_{\Omega} d^3r \left[\frac{K}{2} (\partial_i p_i)^2 - h_{\parallel}^0 p_i p_i \right] + \int_{\Sigma} dS f_s , \quad (3)$$

where K is the elastic constant and h_{\parallel}^0 is a Lagrange multiplier ensuring $|\mathbf{p}| = 1$. Since we are modelling a finite droplet, the surface terms are important. We consider normal anchoring of the filaments to the interface, with surface distortion free energy density $f_s = W(\mathbf{p} \cdot \hat{\mathbf{n}} - 1)^2$.

The polarisation flux is

$$\dot{\boldsymbol{p}} = -\left(\boldsymbol{v}\cdot\nabla\right)\boldsymbol{p} - \underline{\underline{\omega}}\cdot\boldsymbol{p} - \nu\underline{\underline{u}}\cdot\boldsymbol{p} + \frac{\boldsymbol{h}}{\Gamma} \tag{4}$$

where $\omega_{ij} = (\partial_i v_j - \partial_j v_i)/2$ and Γ is the rotational viscosity.

RESULTS

Active Fluid Interface: Linear Instability

In this section we present the results of a linear perturbation to the stationary ground state of the droplet. The system is in a stationary (velocity v = 0) steady state when the interface is spherical (fixed radius $R = R_0$) with a homogeneous concentration of active particles $(c = c_0)$. Then the bulk concentration is $\rho = k_{\rm off} c_0/k_{\rm on}$ inside the drop, and the hydrostatic pressure inside is $P = P_{\rm ext} + (2\gamma_0 - \zeta c_0)/R_0$ where $P_{\rm ext}$ is the stationary state pressure in the external fluid. We perform a linear stability analysis by applying a small perturbation to the variables defined at the interface R and c of the form: $\tilde{g} = g_0 + \sum_{l=1}^{\infty} \sum_{m=-l}^{l} \delta g_{lm}(t) Y_l^m(\theta, \phi)$, where Y_l^m are the spherical harmonic functions and $\delta g_{lm} \ll g_0$. To first order, the resulting flow is given by Lamb's solutions for flow around a sphere, which can be expressed as vector spherical harmonics [30]. Solving the Stokes equation with flow and stress continuity conditions at the droplet interface gives expressions for $\delta v_{lm}^{(i)}$ (as defined in [31] and Supplementary Information appendix A) in terms of δc_{lm} and δR_{lm} . The perturbation on the interface is also coupled to a perturbation of the internal concentration ρ such that

$$\tilde{\rho} = \left[\frac{k_{\text{off}} c_0}{k_{\text{on}}} + \sum_{l=1}^{\infty} \sum_{m=-1}^{l} \delta \rho(r, t) Y_l^m \right].$$

We obtain analytical solutions for the stability in the quasistatic state for ρ (taking $\dot{\rho}=0$). These coupled linear equations are solved exactly with Bessel functions as in [11], however these solutions inhibit the calculation of an analytical stability condition, hence we do not consider them here, but instead compare our approximate analytical solutions directly with the full dynamical simulations.

Finally, we evaluate the coupled system of dynamic equations for the concentration (equation (1) in Methods section) and radius $\dot{R} = \boldsymbol{V}.\boldsymbol{n}$ (the normal velocity at the interface) to first order in the perturbations. We find instabilities by looking for positive eigenvalues of the stability matrix that relates \dot{c} and \dot{R} to δc and δR to first order in the perturbations (see Supplementary Information appendix A for further details of this calculation). From this analysis we find an instability threshold for the effective activity $\tilde{\zeta} < \alpha_I$ where

$$\alpha_I = -\frac{2\tilde{\eta}}{c_0} (2l+1) \left(\frac{D}{R_0} + \frac{D_b R_0 k_{\text{off}}}{(l+1) (D_b l + k_{\text{on}} R_0)} \right), (5)$$

where $\tilde{\eta} = (\eta_0 + \eta_1)/2$ is the mean viscosity of the internal and external fluid. We see that α_I is independent of the effective surface tension γ'_0 which shows that the coupled droplet deformation does not contribute to the symmetry breaking threshold. However, the corresponding

maximum eigenvalue of the stability matrix does weakly depend on the effective surface tension γ_0' for l>1. This weak positive relation suggests that the instability should evolve more quickly in large surface tension drops when l>1. We see that in this linear limit there is no contribution from the advection term in equation (2) so the second term in equation (5) always increases the threshold. This is because the binding terms allows the concentration on the interface to be recycled by unbinding and diffusing into the bulk of the drop.

The stability analysis shows that the droplet will deform, and the shape of the initial instability is equally likely to be any combination of the spherical harmonic modes of given l. The maximally unstable mode l_{max} can be found exactly when binding is not included (see figure 2 and Supplementary Information appendix A) which predicts that as contractile activity is increased, the more concentration peaks will be initially formed on the droplet surface. Note that only the l = 1 mode (k = 1 in 2D) produces net propulsion of the droplet (i.e. $\int_{\Sigma} \mathbf{R} \hat{\mathbf{n}} dS \neq 0$), so the lowest energy mode corresponds to front-back symmetry breaking of the droplet profile. When binding is included $(k_{\text{off}} \neq 0)$ the dispersion relation changes, and as we see from equation (5) the active threshold is non-linear in l, and hence higher (non-swimming) modes can have lower thresholds than the l=1 (swimming) mode.

The droplet shape is enslaved to the concentration (as α_I is independent of γ), so we can estimate how the shape will deform due to certain concentration distributions on the interface by solving $\dot{R}=0$ for δR (for l>1). Plotted in figure 2 is an example of these deformations and the associated flow to linear order. Thus, this linear instability analysis can tell us how one expects spontaneous symmetry breaking to occur and evolve for small deviations from the steady state. In order to look at the resulting steady state dynamics we require numerical simulation.

Active Fluid Interface: Comparison with Simulations

We test these analytical results against the 2D simulations developed in [24]. These use an immersed boundary method [32, 33] to represent the active interface explicitly as a Lagrangian mesh which is coupled to the Cartesian mesh for the 2D fluid via a numerical Dirac delta function.

Repeating the stability analysis in 2D, we now take perturbations of the form $g = g_0 + \sum_{k=1}^{\infty} \mathrm{e}^{ik\theta}$. The calculation reveals that surface tension gradients do not deform the drop in 2D (as found in [34]) however the concentration dynamics remain very similar. We compare our predictions in 2D to the results of the Immersed Boundary simulations in figure 3. We run simulations varying the activity, binding rate (taking $k_{\mathrm{off}} = k_{\mathrm{on}}$) and

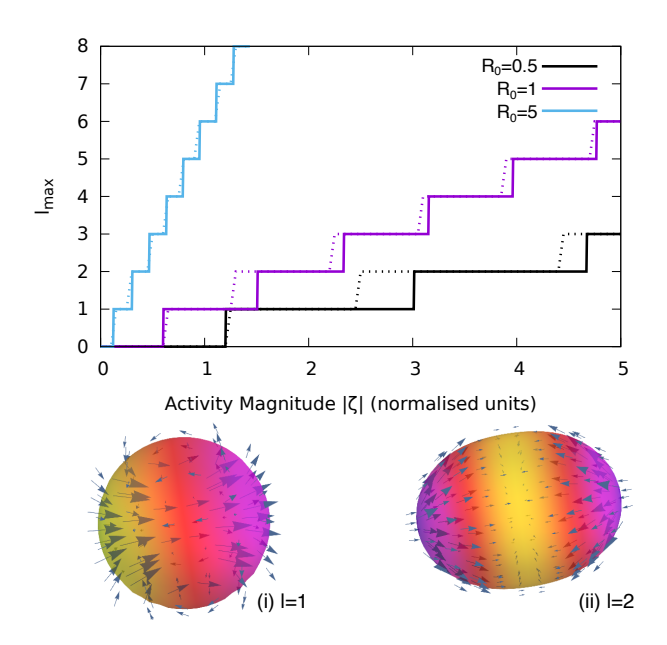


FIG. 2. Maximum mode number l_{max} plotted against activity in normalised units for increasing values of the droplet radius. Dashed lines show numerical solution and solid lines show analytical approximation using $\dot{R}=0$. Parameters used: $c_0=1,\ \gamma_0=1,\ D=0.05,\ \eta_0=\eta_1=1$ and $k_{\text{off}}=0$. Insets show flow (blue arrows) and active concentration c (colour gradient from purple (low) to yellow (high)) to linear order on the perturbed interface for a (i) l=1 mode and (ii) l=2 mode respectively. Deformation of the interface in (ii) is calculated using $\dot{R}=0$ and is exaggerated for clarity by making γ_0' small.

diffusion parameters. At zero binding we observe two steady phases, a stationary state and a steady moving state 3(a) separated by the threshold $\alpha_{\rm I,2D}$ which agrees well with the expected analytical result

$$\alpha_{\rm I,2D} = -4 \frac{\tilde{\eta}}{c_0} \left(\frac{Dk}{R_0} + \frac{D_b R_0 k_{\rm off}}{(D_b k + k_{\rm on} R_0)} \right).$$
 (6)

This moving steady state due to a surface tension gradient is also observed for the the self-propelled droplets studied in [34, 35]. The equations of motion we use (see Model section) are similar to those for the self-propelled droplets studied in [34, 35] and hence some of the same dynamical behaviour is observed. However, our model predicts new stable states and instabilities corresponding to pure deformation and division as discussed below. This arises due to the advection and diffusion of active particles through the bulk of the drop. Unlike in [34, 35] the model here conserves the active particles within the drop making it more relevant to cell cortex dynamics.

We next calculate the maximum mode number $k_{\rm max}$ (see Supplementary Information appendix A). In the regime where we predict $k_{\rm max}=2$, our simulations show initial formation of 2 peaks in droplet concentration. Without binding, these peaks are unstable and always coalesce to form one (as predicted for a flat active viscous layer in [8]. The threshold predicted compares well

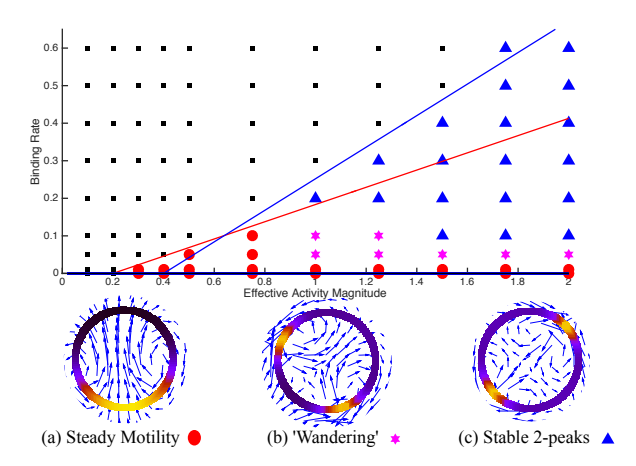


FIG. 3. Phase diagram of 2D simulation results for an active isotropic interface, each dot represents a single simulation run. Insets show steady state flow (blue arrows) and concentration fields (colour density, black to yellow) for the different phases. Low values of $k_{\rm off}$ transition from stationary (black squares) to motile (red circles) with a single peak in concentration (shown in (a)). Feedback from the internal concentration enables wandering states (magenta stars) and a stationary 2-peak state (blue triangles). Solid lines of increasing gradient show predicted activity threshold for modes k=1,2 (blue, red). Simulation parameters: $c_0=1,\ R_0=1,\ \gamma_0=1,\ D=0.05,\ D_b=0.5,\ \eta_0=\eta_1=1.$

to that in the simulations, especially for small values of the binding. As we increase $k_{\rm off}$ and $\tilde{\zeta}$ we see that the resulting motion begins to 'wander', as advection of the internal density away from the droplet rear nucleates new peaks in the concentration profile. Furthermore, it is possible to achieve a state with 2 stable peaks when this coupling is strong enough (see figure 3). Equation (6) predicts a non-trivial k dependence of the active threshold as binding terms become important. This explains the observed non-linear dependence of the threshold on activity in figure 3, demonstrated by lines k=1 and k=2. Note this is very similar to the prediction in 3D in equation (5).

The simulation results in figure 3 demonstrate that as the binding rate increases, advection of the concentration through the droplet bulk becomes more important. The advection can stabilise the two peaks at diametrically opposite points on the circle, resulting in a stationary droplet. However, we see that in 2D the drop does not deform, as the radial forces from the activity gradients are always cancelled by the hydrostatic pressure P. This is not the case for the full 3D system where we expect concentration gradients to deform the droplets as shown in figure 2. Nonetheless, the 2D simulations show that advection can stabilise the 2 peak configuration, which in 3D would result in symmetric deformation and potentially division of the droplet. Such a 3D simulation is beyond the scope of this work, but would be useful for

quantifying the full 3D morphology.

Active Polar Fluid Drop: Linear Stability Analysis

We contrast the model of an active interface to that of a droplet of active polar fluid of constant density. In this case, rather than the concentration of active particles, the important degree of freedom is the polarisation vector \boldsymbol{p} denoting the average direction of the contractile filaments in the fluid.

We calculate the linear stability of the droplet in the limit of strong anchoring $W \to \infty$ in order to study the effects between the coupling of droplet morphology and polarisation. In the case of weak or no anchoring, instabilities can occur for both extensile ($\zeta > 0$) and contractile ($\zeta < 0$) active polar drops as shown analytically in [36] and in simulations [15]. The condition of fixed polarisation at the interface inhibits certain deformations of the polarisation field at low activities and so the preferred deformation modes are those which can couple to the droplet deformation. This was demonstrated in 2D simulations of active nematic drops in [17]. Here we explain this mechanism analytically in a 3D fluid drop by linear stability analysis. The polar nature of the anchoring produces a "radial hedgehog" topological defect at the droplet centre (or a radial defect with +1 winding number in 2D), giving a simple analytical description of the stationary state. Thus we are able to make analytical predictions about spontaneous symmetry breaking in these systems even in the general 3D case.

Unlike the case of an active interface, the active fluid here fills the drop, and hence active and passive stresses are generated in the bulk. The stationary steady state is given by the polarisation $\mathbf{p} = \hat{\mathbf{r}}, \mathbf{R} = R_0 \hat{\mathbf{r}}, \mathbf{v} = 0,$ and the Lagrange multiplier $h_{\parallel}^0 = -2K/r^2$ (see Model section). Due to the symmetry of the stationary state, we first need to consider the special case of the translational mode of perturbation, corresponding to the l=1spherical harmonic mode. Without loss of generality we consider a perturbation along the z-direction (m = 0). This mode implies a translation of the hedgehog defect away from the droplet centre. If we assume that the defect has some finite core radius R_c then we can treat the liquid crystal as contained between two boundary conditions, one at $r = R_c \equiv R_{c0} + \delta z Y_1^0(\theta, \phi)$ and one at $r=R_0$ for some small perturbation distance δz . In the equilibrium case, we can write a polarisation field to first order that minimises the bulk free energy in equation (3) by solving $h_{\perp} \equiv h - (h \cdot n)n = 0$ for these boundary boundary conditions. To first order in δz this gives

$$\boldsymbol{p}_{l=1} = \boldsymbol{e}_r - \delta z \frac{R_0 - r}{r(R_0 - R_{c0})} \left(\partial_{\theta} Y_1^0 \boldsymbol{e}_{\theta} + \frac{1}{\sin(\theta)} \partial_{\phi} Y_1^0 \boldsymbol{e}_{\phi} \right) .$$

Note this is divergent at the origin of our coordinate system as this is not a continuous deformation around the

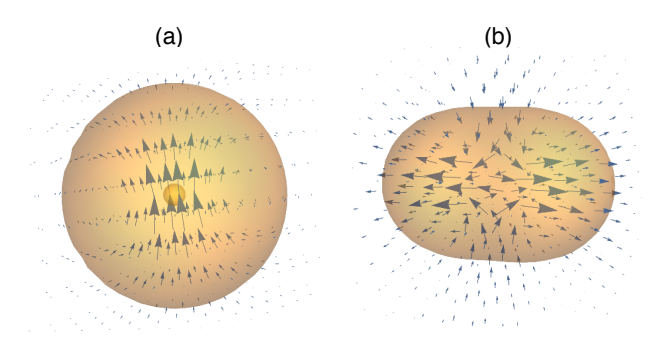


FIG. 4. Active part of the flow field (blue arrows) to linear order of active polar droplet for: (a) defect position (inner sphere) perturbed in the vertical direction with $\zeta>0$ (extensile activity); (b) l=2 mode perturbation of the interface assuming strong anchoring of the polarisation field with $\zeta>0$ (contractile activity). The perturbations are made artificially large for visibility here.

defect. Solving for the flow by applying stress and velocity continuity at the interface, we integrate to find the velocity of the defect core and droplet (for details see Supplementary Information appendix B). Then the relative velocity of the defect is:

$$\Delta V \equiv V_c - V_{\text{drop}} \approx \zeta \sqrt{\frac{3}{\pi}} \delta z \frac{R_0(2\eta_0 + \eta_1) - R_{c0}(\eta_0 + \eta_1)}{4R_0\eta_0(3\eta_0 + 2\eta_1)}.$$

We see for extensile activity, the defect always moves in the same direction as the perturbation relative to the drop (see figure 4), which suggests that extensile activity will destabilise the defect from the centre and give rise to motion of the droplet as a whole. Conversely, we expect contractile activity to stabilise the defect at the droplet centre. There is an energy cost to deformations of this form, and hence there is a restoring force proportional the the Frank elastic constant, so within these assumptions one can predict that the droplet will break translational symmetry spontaneously above some finite activity proportional to K and dependent on R_{c0} (for details see the Supplementary Information appendix B). This predicted threshold is very sensitive to the defect core radius R_{c0} and so it is difficult to make a quantitative prediction. Qualitatively however this describes the phase transition we observe in the simulations for extensile activity.

For perturbation modes l > 1 the flow at the origin will always be zero, and so one can assume that in the strong anchoring limit the defect will remain centred at the origin. Ideally then we would consider a generic small perturbation to the steady state polarisation field. However, this is not analytically tractable even to linear order due to coupling with the fluid flow. Thus, we consider the case where the deformation of the polarisation field is proportional to the lowest order term in r allowed by continuity considerations, in 3D this is r^0 . This is an approximation which allows us to consider the dynamics if

filament polarisation at the interface and in the droplet are strongly coupled. However it comes at the cost of reducing the quantitative power of our predictions. In the strong anchoring limit, the polarisation has to match the perturbed interface normal at r=R to first order, such that

$$\boldsymbol{p} = \hat{\boldsymbol{r}} - \sum_{l=2}^{\infty} \sum_{m=-l}^{l} \left[\frac{\delta R_{lm}(t)}{R_0} r(\nabla Y_l^m(\theta, \phi)) \right]. \tag{7}$$

We calculate the resulting flows to first order in δR . Since p is enslaved to the deformation we then only need to consider the radius dynamics given by \dot{R} (for details see appendix).

In this strong anchoring limit we find that the droplet is unstable if $\zeta < \alpha_P < 0$, i.e. the activity threshold, α_P , is always contractile. The threshold α_P increases linearly with γ and K. Repeating the linear stability analysis calculation in 2D shows the same qualitative prediction, where this time we take $\delta p \propto r$ as this is the leading order contribution allowed. The analytical expressions for the activity threshold are given in Supplementary Information appendix C and a full discussion of the eigenvalues of the general stability matrix (for weak anchoring) can be found in [36].

The result of this analysis is somewhat surprising, in this strong anchoring limit we expect the l=1 mode to be unstable to extensile activity, whereas the higher modes of deformation are unstable for contractile activity. This suggests that, when our assumptions hold, we should see translational symmetry breaking with the defect moving to the droplet front for an extensile drop and symmetric modes of deformation for a contractile drop (see figure 4). This active threshold scales linearly with K and γ_0 , demonstrating the importance of the coupling of the morphology to the polarisation field. Contrast this to the case of the active interface where the shape does not affect the threshold for a phase transition.

This contractile instability can be understood physically by considering the splay in the drop due to perturbations in the interface curvature. High curvature couples to increased splay which couples to outward flow, further increasing the curvature of the interface and hence the splay.

Active Polar Fluid Drop: Comparison with Simulations

In the 2D simulations (see figure 5) we see symmetry breaking corresponding to the k=1 mode for extensile activity resulting in a steady motile state, as predicted by the stability analysis. This is characterised by the defect centre moving to the front of the drop and is independent of the boundary deformation (and hence γ_0). Conversely contractile activity stabilises the defect at the

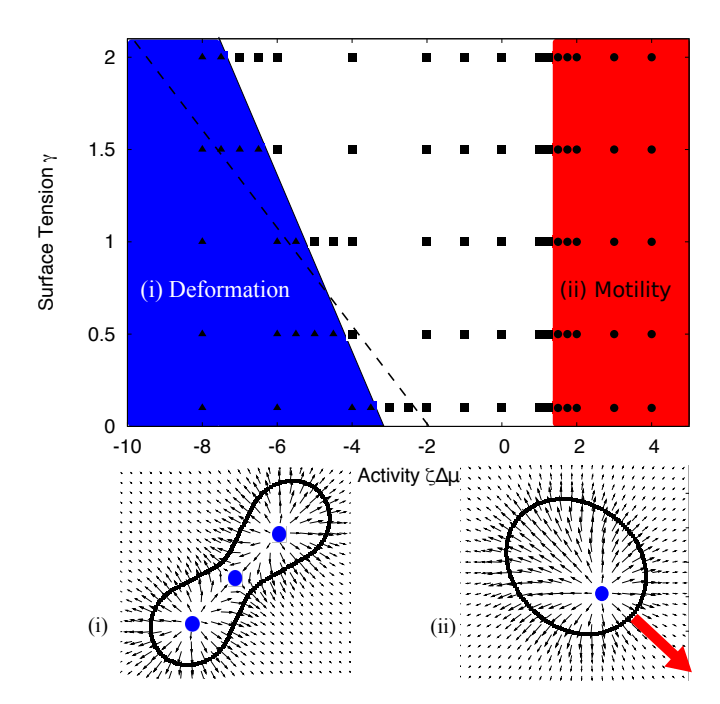


FIG. 5. Active polar drop stability diagram. Stationary state (white, square dots), spontaneous symmetric deformation (blue, triangular dots) and spontaneous motility (red, round dots) are observed. Dashed line shows analytical prediction from linear stability analysis. Insets show the polarisation field \boldsymbol{p} (black arrows) inside the droplet following symmetry breaking with defects labelled by blue dots. Parameters: $K=0.1,\ R_0=1,\ \eta_0=\eta_1=\Gamma=1,\ W=50$ and $\nu=1.1$.

droplet centre and we observe a k=2 mode instability characterised by deformation of the droplet into a 'dumbbell' shape. It is also observed that this phase behaviour breaks down as the value of K/R_0^2 is reduced. In this limit the distortions in the droplet bulk are not strongly coupled to those at the interface and so more complex distortions can occur without significant droplet deformation. Our analytical calculations do not predict this as we assume a form for the r-dependence of the polarisation such that it is strongly coupled to the curvature. This behaviour goes beyond the scope of the analytical work here as this corresponds to a transition to an 'active turbulence' state, as numerically simulated in [24].

Finally, we also observe rotational steady states in the simulations (for extensile activity when using $\nu=-1.1$) which can be characterised exactly by rotationally invariant distortions [2, 3], but these are not predicted for the parameter range used in figure 5.

DISCUSSION

We have used analytical linear stability analysis and numerical simulation to characterise instabilities and their resulting non-equilibrium steady states. Recent advances in experimental techniques mean that active gels of cytoskeletal material can be produced *in vitro*. The predictions of our active interface model could be tested by adsorbing an isotropic actin gel onto the interface of an emulsion drop containing myosin and ATP. We predict an activity threshold for spontaneous motion, and a further continuous transition to a stable symmetric mode mediated by advection of motors through the droplet bulk. We predict that in 3D this symmetric mode will be coupled to deformation of the drop, however this cannot be observed in the 2D model.

The active polar gel model described here may only capture aspects of the full dynamics of such a system where filament polymerisation and motor density fluctuations can be of importance. However, this model system gives us an insight into the intrinsic instabilities when droplet deformation and filament direction are strongly coupled. In particular, there is a contractile activity threshold that is linearly dependent on surface tension, above which the droplet spontaneously deforms into a characteristic dumbbell shape. We also see persistent motility in the case of extensile activity such that the droplet acts as a pusher, compared to the puller type motion exhibited in the active isotropic interface model. An interesting future extension of this work would be to consider coupling between both active phases in a single drop.

The finite active systems we study improve our understanding of how confinement and deformation affect steady state dynamics. Additionally, we see the importance of feedback, driven by advection through the droplet or the internal orientational order, resulting in more complex dynamics. These results should prove useful in characterising future experiments on *in vitro* cytoskeletal networks and be useful in developing more complex models of multicomponent active systems in nature.

We acknowledge the EPSRC for funding this work, grant reference EP- K503149-1.

- * Corresponding author: carl.whitfield@physics.org; Current address: Department of Physics, University of Warwick, Coventry, UK, CV3 7AL
- M. C. Marchetti, J.-F. Joanny, S. Ramaswamy, T. B. Liverpool, J. Prost, M. Rao, and R. A. Simha, Rev. Mod. Phys. 85, 1143 (2013), arXiv:1207.2929.
- [2] K. Kruse, J.-F. Joanny, F. Jülicher, J. Prost, and K. Sekimoto, Phys. Rev. Lett. 92, 078101 (2004).
- [3] K. Kruse, J.-F. Joanny, F. J\"{u}licher, J. Prost, and K. Sekimoto, Eur. Phys. J. E **16**, 5 (2005), arXiv:0406058v1 [arXiv:physics].
- [4] S. Fürthauer, M. Neef, S. W. Grill, K. Kruse, and F. Jülicher, New J. Phys. 14, 023001 (2012).
- [5] R. Voituriez, J.-F. Joanny, and J. Prost, Europhys. Lett. 70, 404 (2005).

- [6] R. Voituriez, J.-F. Joanny, and J. Prost, Phys. Rev. Lett. 96, 028102 (2006).
- [7] K. Kruse, J.-F. Joanny, F. Jülicher, and J. Prost, Phys. Biol. 3, 130 (2006).
- [8] J. S. Bois, F. Jülicher, and S. W. Grill, Phys. Rev. Lett. 106, 028103 (2011).
- [9] N. Sarkar and A. Basu, Phys. Rev. E 92, 052306 (2015).
- [10] A. Zumdieck, M. C. Lagomarsino, C. Tanase, K. Kruse, B. Mulder, M. Dogterom, and F. Jülicher, Phys. Rev. Lett. 95, 258103 (2005).
- [11] R. J. Hawkins, R. Poincloux, O. Bénichou, M. Piel, P. Chavrier, and R. Voituriez, Biophys. J. 101, 1041 (2011).
- [12] J.-F. Joanny, K. Kruse, J. Prost, and S. Ramaswamy, Eur. Phys. J. E 36, 52 (2013), arXiv:1302.5025.
- [13] D. Khoromskaia and G. P. Alexander, Phys. Rev. E 92, 062311 (2015), arXiv:1508.05242.
- [14] A. C. Callan-Jones, J.-F. Joanny, and J. Prost, Phys. Rev. Lett. 100, 258106 (2008).
- [15] E. Tjhung, D. Marenduzzo, and M. E. Cates, PNAS 109, 12381 (2012).
- [16] J.-F. Joanny and S. Ramaswamy, J. Fluid Mech. 705, 46 (2012).
- [17] L. Giomi and A. DeSimone, Phys. Rev. Lett. 112, 147802 (2014).
- [18] C. A. Whitfield, D. Marenduzzo, R. Voituriez, and R. J. Hawkins, Eur. Phys. J. E 37, 8 (2014), arXiv:1307.3426.
- [19] W. Marth, S. Praetorius, and A. Voigt, J. R. Soc. Interface 12, 20150161 (2015), arXiv:1412.5296.
- [20] R. J. Hawkins, M. Piel, G. Faure-Andre, A. M. Lennon-Dumenil, J. F. Joanny, J. Prost, and R. Voituriez, Phys. Rev. Lett. 102, 058103 (2009).
- [21] F. G. Woodhouse and R. E. Goldstein, Phys. Rev. Lett. 109, 168105 (2012).
- [22] A. C. Callan-Jones and R. Voituriez, New J. Phys. 15, 025022 (2013).
- [23] A. Kumar, A. Maitra, M. Sumit, S. Ramaswamy, and G. V. Shiyashankar, Sci. Rep. 4, 3781 (2014).
- [24] C. A. Whitfield and R. J. Hawkins, arXiv Prepr. (2016), arXiv:1605.01621.
- [25] P. M. Bendix, G. H. Koenderink, D. Cuvelier, Z. Dogic, B. N. Koeleman, W. M. Brieher, C. M. Field, L. Mahadevan, and D. a. Weitz, Biophys. J. 94, 3126 (2008).
- [26] T. Sanchez, D. T. N. Chen, S. J. DeCamp, M. Heymann, and Z. Dogic, Nature 491, 431 (2012).
- [27] F. C. Keber, E. Loiseau, T. Sanchez, S. J. DeCamp, L. Giomi, M. J. Bowick, M. C. Marchetti, Z. Dogic, and A. R. Bausch, Science 345, 1135 (2014), arXiv:1409.1836.
- [28] J. Löber, F. Ziebert, and I. S. Aranson, Sci. Rep. 5, 9172 (2015).
- [29] F. Ziebert and I. S. Aranson, Eur. Phys. J. Spec. Top. 223, 1265 (2014).
- [30] S. H. Lamb, *Hydrodynamics* (Courier Corporation, 1945).
- [31] B. Carrascal, G. a. Estevez, P. Lee, and V. Lorenzo, Eur. J. Phys. 12, 184 (1991).
- [32] C. S. Peskin, Acta Numer. 11, 479 (2002).
- [33] M.-C. Lai, Y.-H. Tseng, and H. Huang, J. Comp. Phys. 227, 7279 (2008).
- [34] N. Yoshinaga, Phys. Rev. E 89, 012913 (2014), arXiv:1307.3120.
- [35] T. Ohta and T. Ohkuma, Phys. Rev. Lett. 102, 154101 (2009).
- [36] C. A. Whitfield, Modelling Spontaneous Motion and Deformation of Active Droplets, Ph.D. thesis, University of

Sheffield (2015).

SUPPLEMENTARY INFORMATION: APPENDICES

Appendix A: Flow field and Stability of Active Interface.

The generic perturbation to the active interface model is of the form:

$$c = c_0 + \sum_{l=1}^{\infty} \sum_{m=-l}^{l} \delta c_{lm} Y_l^m(\theta, \phi),$$
 (S.1)

$$\boldsymbol{v} = \sum_{l=1}^{\infty} \sum_{m=-l}^{l} \left[\delta v_{lm}^{(1)}(r) Y_{l}^{m}(\theta, \phi) \hat{\boldsymbol{r}} + \delta v_{lm}^{(2)}(r) r(\nabla Y_{l}^{m}(\theta, \phi)) + \delta v_{lm}^{(3)}(r) \left(\boldsymbol{r} \times \nabla Y_{l}^{m}(\theta, \phi) \right) \right], \tag{S.2}$$

$$\mathbf{R} = R\hat{\mathbf{e}}_r = \left\{ R_0 + \sum_{l=1}^{\infty} \sum_{m=-l}^{l} \delta R_{lm} Y_l^m(\theta, \phi) \right\} \hat{\mathbf{e}}_r , \qquad (S.3)$$

$$P = P_0 + \sum_{l=1}^{\infty} \sum_{m=-l}^{l} \delta P_{lm}(r) Y_l^m(\theta, \phi) .$$
 (S.4)

where we assume the perturbations $\delta g_{l,m} \ll 1$ for $g = c, v^{(i)}$, and R. Note that all real perturbations will satisfy the constraint $\delta g_{lm} = (-1)^m \delta g_{l,-m}^*$. From equation (S.3) we can calculate the perturbed normal and tangential vectors to first order in δR_{lm} :

$$\hat{\boldsymbol{n}} = \hat{\boldsymbol{e}}_r - \sum_{l=1}^{\infty} \sum_{m=-l}^{l} \frac{\delta R_{lm}}{R_0} \left[\frac{\partial Y_l^m}{\partial \theta} \hat{\boldsymbol{e}}_{\theta} + \frac{1}{\sin(\theta)} \frac{\partial Y_l^m}{\partial \phi} \hat{\boldsymbol{e}}_{\phi} \right], \tag{S.5}$$

$$\hat{\boldsymbol{t}}_{1} = \left[\sum_{l=1}^{\infty} \sum_{m=-l}^{l} \frac{\delta R_{lm}}{R_{0}} \frac{\partial Y_{l}^{m}}{\partial \theta} \right] \hat{\boldsymbol{e}}_{r} + \hat{\boldsymbol{e}}_{\theta} , \qquad (S.6)$$

$$\hat{\boldsymbol{t}}_{2} = \left[\sum_{l=1}^{\infty} \sum_{m=-l}^{l} \frac{\delta R_{lm}}{R_{0}} \frac{1}{\sin(\theta)} \frac{\partial Y_{l}^{m}}{\partial \phi} \right] \hat{\boldsymbol{e}}_{r} + \hat{\boldsymbol{e}}_{\phi} . \tag{S.7}$$

Substituting (S.1) and (S.3) into the expression for the force on the interface gives:

$$\begin{aligned} \boldsymbol{F}_{lm} &= -\frac{1}{R_0} \left\{ 2\gamma_0' + \left[\gamma_0'(l+2)(l-1) \frac{\delta R_{lm}}{R_0} - 2\delta c_{lm} \tilde{\zeta} \right] Y_l^m \right\} \hat{\boldsymbol{e}}_r \\ &+ \frac{1}{R_0} \left[2\gamma_0' \frac{\delta R_{lm}}{R_0} - \tilde{\zeta} \delta c_{lm} \right] \frac{\partial Y_l^m}{\partial \theta} \hat{\boldsymbol{e}}_\theta + \frac{1}{R_0 \sin(\theta)} \left[2\gamma_0' \frac{\delta R_{lm}}{R_0} - \tilde{\zeta} \delta c_{lm} \right] \frac{\partial Y_l^m}{\partial \phi} \hat{\boldsymbol{e}}_\phi \end{aligned} \tag{S.8}$$

where $\gamma_0' = \gamma_0 - \tilde{\zeta}c_0 - Bc_0^2/2$ and $\tilde{\zeta} = \zeta + Bc_0$ as defined in the text. As this force is located at the interface, we can solve the fluid flow in the bulk with Lamb's general solutions for flow around a sphere, which defines the $\delta v_{lm}^{(i)}$ and δP_{lm} functions:

$$\delta v_{lm}^{(1)}(r) = \begin{cases} a_{lm}^{(0)} r^{l+1} + a_{lm}^{(1)} r^{l-1} & \text{if } r < R \\ b_{lm}^{(0)} r^{-l} + b_{lm}^{(1)} r^{-l-2} & \text{if } r > R \end{cases}$$
(S.9)

$$\delta v_{lm}^{(2)}(r) = \begin{cases} \left(a_{lm}^{(0)}(l+3)r^{l+1} + a_{lm}^{(1)}(l+1)r^{l-1} \right) / [l(l+1)] & \text{if } r < R \\ - \left(b_{lm}^{(0)}(l-2)r^{-l} + b_{lm}^{(1)}lr^{-l-2} \right) / [l(l+1)] & \text{if } r > R \end{cases}$$
(S.10)

$$\delta v_{lm}^{(3)}(r) = \begin{cases} a_{lm}^{(2)} r^l & \text{if } r < R \\ b_{lm}^{(2)} r^{-l-1} & \text{if } r > R \end{cases}$$
(S.11)

$$\delta v_{lm}^{(3)}(r) = \begin{cases} a_{lm}^{(2)} r^l & \text{if } r < R \\ b_{lm}^{(2)} r^{-l-1} & \text{if } r > R \end{cases}$$

$$\delta P_{lm}(r) = \begin{cases} 2\eta_0 a_{lm}^{(0)} r^l (2l+3)/l & \text{if } r < R \\ 2\eta_1 b_{lm}^{(0)} r^{-l-1} (2l-1)/(l+1) & \text{if } r > R \end{cases}$$
(S.11)

We can then find the coefficients $a_{lm}^{(i)}$ and $b_{lm}^{(i)}$ by solving the boundary conditions of flow and stress continuity (or force balance), including the contribution from the active interface:

$$\left. \boldsymbol{v}^{\text{ext}} \right|_{r=R} - \left. \boldsymbol{v} \right|_{r=R} = 0$$
 (S.13)

$$2\hat{\boldsymbol{n}} \cdot \left[\eta_0 \underline{\underline{\boldsymbol{u}}} - \eta_1 \underline{\underline{\boldsymbol{u}}}^{\text{ext}} \right] \Big|_{r=R} = \boldsymbol{F}_{lm} + (P - P^{\text{ext}}) \hat{\boldsymbol{n}} \Big|_{r=R}$$
(S.14)

where $\underline{\underline{u}} = (\nabla v + (\nabla v)^{\mathrm{T}})/2$ is the strain rate tensor and the superscript 'ext' denotes a property of the external fluid Ω_1 . Solving these for the flow and pressure from equations (S.9)-(S.12) we find:

$$a_{lm}^{(0)} = \frac{l(l+1)(l+2)}{2\eta'} \left[\gamma_0' \frac{\delta R_{lm}}{R_0} (l-1) - \tilde{\zeta} \delta c_{lm} \right] R_0^{-l-1}$$
(S.15)

$$b_{lm}^{(0)} = -\frac{l(l+1)(l-1)}{2\eta^*} \left[\gamma_0' \frac{\delta R_{lm}}{R_0} (l+2) + \tilde{\zeta} \delta c_{lm} \right] R_0^l$$
(S.16)

$$a_{lm}^{(1)} = -\frac{l(l+1)}{2\eta'\eta^*} \left\{ \gamma_0' \frac{\delta R_{lm}}{R_0} (l+2)(l-1) \left[3\eta_1 + 4\tilde{\eta}l(l+2) \right] - \tilde{\zeta}\delta c_{lm} \left[6(\eta_1 - \eta_0) + 3l\eta_1 + 4\tilde{\eta}l^2(l+2) \right] \right\} R_0^{-l+1}$$
 (S.17)

$$b_{lm}^{(1)} = \frac{l(l+1)}{2\eta'\eta^*} \left\{ \gamma_0' \frac{\delta R_{lm}}{R_0} (l+2)(l-1)(\eta_0 - 2\eta_1 + 4l^2\tilde{\eta}) + \tilde{\zeta}\delta c_{lm} \left[4\eta_1 - 5\eta_0 + l(\eta_0 - 2\eta_1) + 4l^2(l+1)\tilde{\eta} \right] \right\} R_0^{l+2} \quad (S.18)$$

$$a_{lm}^{(2)} = b_{lm}^{(2)} = 0. (S.19)$$

where $\eta' = [3\eta_0 + 4\tilde{\eta}l(l+2)]$ and $\eta^* = (\eta_1 - 2\eta_0 + 4l^2\tilde{\eta})$, and $\tilde{\eta} = (\eta_0 + \eta_1)/2$ as in the text. In order to satisfy the binding and unbinding dynamics, we consider the limit $\dot{\rho} = 0$, which gives $\delta\rho_{lm}(r,t) = \delta c_{lm}k_{\rm off}R_0^{(1-l)}r^l/(D_bl + k_{\rm on}R_0)$. We then use these solutions in the dynamic equations (1) and $\dot{R} = V.n$ which can be written in matrix form as:

$$\frac{\mathrm{d}}{\mathrm{d}t} \begin{pmatrix} \delta c_{lm} \\ \delta R_{lm} \end{pmatrix} = \underline{\underline{T}} \begin{pmatrix} \delta c_{lm} \\ \delta R_{lm} \end{pmatrix}$$
where
$$\underline{\underline{T}} = \begin{pmatrix} X - \tilde{\zeta}(c_0/R_0)(4\eta_1 - 5\eta_0 + 2l^2(l+3)\tilde{\eta})Y & \frac{\gamma_0'c_0}{R_0^2}(l+2)(l-1)(2\eta_1 - \eta_0 + 2l\tilde{\eta})Y \\ \tilde{\zeta}(2\eta_1 - \eta_0 + 2l\tilde{\eta})Y & -2\frac{\gamma_0'}{R_0}(l+2)(l-1)\tilde{\eta}Y \end{pmatrix}$$
(S.20)

where $X = -Dl(l+1)/R_0^2 - D_b k_{\text{off}} l/(D_b l + k_{\text{on}} R_0)$ and $Y = l(l+1)/(\eta' \eta^*)$. Clearly, when l=1, there is no deformation and the eigenvalue λ of $\underline{\underline{T}}$ is just equal to T_{11} . In general the solution for the eigenvalues is the root of a quadratic. One of the eigenvalues is always zero when $\gamma'_0 = 0$, and is positive for $\gamma'_0 < 0$. This instability corresponds to a droplet with a negative bare surface tension. The other solution for $\lambda = 0$ corresponds to

$$\tilde{\zeta} = \alpha_I \equiv -\frac{2(2l+1)\tilde{\eta}}{c_0} \left(\frac{D}{R_0} + \frac{D_b R_0 k_{\text{off}}}{(l+1)(D_b l + k_{\text{on}} R_0)} \right)$$
 (S.21)

as given in the text. We see that the expression for λ in terms of l is complicated. However, since α_I does not depend on the bare surface tension γ'_0 the instability threshold does not depend on the deformation. Thus, we can find an approximate expression for λ by solving $\dot{R} = 0$ for δR_{lm} , which gives:

$$\delta R_{lm}^* = \frac{\tilde{\zeta} R_0 \delta c_{lm}}{2\gamma_0'(l+2)(l-1)}.$$
 (S.22)

Substituting this for δR_{lm} in equation (1) we find:

$$\frac{\mathrm{d}\delta c_{lm}^*}{\mathrm{d}t} = -\left[\frac{l(l+1)}{R_0^2} \left(\frac{\tilde{\zeta}c_0R_0}{2(2l+1)\tilde{\eta}} + D\right) + \frac{D_bk_{\mathrm{off}}l}{D_bl + k_{\mathrm{on}}R_0}\right]\delta c_{lm}^* \equiv \lambda^*\delta c_{lm}^*. \tag{S.23}$$

The resulting equation for $\partial \lambda^*/\partial l = 0$ is a fifth order polynomial in l, this simplifies to a cubic equation in the limit $k_{\text{off}} \to 0$. The solution to this cubic equation is the analytical line plotted in figure 2. As shown in equation (S.21), the activity threshold does not increase linearly with l if $k_{\text{off}} \neq 0$.

In 2-dimensions, the general solutions for flow around a circle are:

$$v_r = \begin{cases} \sum_{k=1}^{\infty} \left(a_k^{(0)} r^{k+1} + a_k^{(1)} r^{k-1} \right) e^{ik\theta} & \text{if } r < R_0 \\ \sum_{k=1}^{\infty} \left(b_k^{(0)} r^{-k+1} + b_k^{(1)} r^{-k-1} \right) e^{ik\theta} & \text{if } r > R_0 \end{cases}$$
(S.24)

$$v_{r} = \begin{cases} \sum_{k=1}^{\infty} \left(a_{k}^{(0)} r^{k+1} + a_{k}^{(1)} r^{k-1} \right) e^{ik\theta} & \text{if } r < R_{0} \\ \sum_{k=1}^{\infty} \left(b_{k}^{(0)} r^{-k+1} + b_{k}^{(1)} r^{-k-1} \right) e^{ik\theta} & \text{if } r > R_{0} \end{cases}$$

$$v_{\theta} = \begin{cases} i \sum_{k=1}^{\infty} \left[(k+2) a_{k}^{(0)} r^{k+1} + k a_{k}^{(1)} r^{k-1} \right] e^{ik\theta} / k & \text{if } r < R_{0} \\ -i \sum_{k=1}^{\infty} \left[(k-2) b_{k}^{(0)} r^{-k+1} + k b_{k}^{(1)} r^{-k-1} \right] e^{ik\theta} / k & \text{if } r < R_{0} \end{cases}$$

$$P = \begin{cases} P_{0} + 4 \eta_{0} \sum_{k=1}^{\infty} (k+1) a_{k}^{(0)} r^{k} e^{ik\theta} / k & \text{if } r < R_{0} \\ P_{0}^{\text{ext}} + 4 \eta_{1} \sum_{k=1}^{\infty} (k-1) b_{k}^{(0)} r^{-k} e^{ik\theta} / k & \text{if } r > R_{0} \end{cases}$$
(S.26)

$$P = \begin{cases} P_0 + 4\eta_0 \sum_{k=1}^{\infty} (k+1)a_k^{(0)} r^k e^{ik\theta} / k & \text{if } r < R_0 \\ P_0^{\text{ext}} + 4\eta_1 \sum_{k=1}^{\infty} (k-1)b_k^{(0)} r^{-k} e^{ik\theta} / k & \text{if } r > R_0 \end{cases},$$
 (S.26)

where r and θ are plane polar coordinates.

Applying the perturbation to the concentration and solving the boundary conditions of continuous velocity and force balance at the interface we can solve for the constants $a_k^{(i)}, b_k^{(i)}$ and find:

$$a_k^{(0)} = -\frac{k}{4R_0^{k+1}(\eta + \eta^{\text{ext}})} \left(\tilde{\zeta} \delta c_k - (k-1)\gamma_0' \frac{\delta R_k}{R_0} \right)$$
 (S.27)

$$a_k^{(1)} = \frac{k}{4R_0^{k-1}(\eta + \eta^{\text{ext}})} \left(\tilde{\zeta} \delta c_k - (k+1) \gamma_0' \frac{\delta R_k}{R_0} \right)$$
 (S.28)

$$b_k^{(0)} = -\frac{kR_0^{k-1}}{4(\eta + \eta^{\text{ext}})} \left(\tilde{\zeta} \delta c_k + (k+1) \gamma_0' \frac{\delta R_k}{R_0} \right)$$
 (S.29)

$$b_k^{(1)} = \frac{kR_0^{k+1}}{4(\eta + \eta^{\text{ext}})} \left(\tilde{\zeta} \delta c_k + (k-1)\gamma_0' \frac{\delta R_k}{R_0} \right)$$
 (S.30)

On substitution of these into the dynamic equations for c and R, we see that the deformation does not depend on δc_k , and hence the droplet shape is always stable as a circle for positive effective surface tension ($\gamma'_0 > 0$). This means that the only instability comes from the dynamics of c on the surface:

$$\frac{\partial \delta c_k}{\partial t} = k \left\{ -\frac{\tilde{\zeta} c_0}{2R_0 \tilde{\eta}} - \frac{Dk}{R_0^2} - \frac{D_b k_{\text{off}}}{D_b k + k_{\text{on}} R_0} \right\} \delta c_k \equiv \lambda_{2D} \delta c_k$$
 (S.31)

leading to the active threshold in equation (6). The maximally unstable mode can again be found by solving for the zeros in the gradient of the dispersion relation $\partial \lambda_{2D}/\partial k = 0$. The expressions for k_{max} are the solutions to the cubic equation:

$$\left[4DD_b^2\tilde{\eta}\right]k^3 + \left[D_bR_0\left(\tilde{\zeta}D_bc_0 + 8Dk_{\rm on}\tilde{\eta}\right)\right]k^2 + \left[2k_{\rm on}R_0^2\left(\tilde{\zeta}D_bc_0 + 2Dk_{\rm on}\tilde{\eta}\right)\right]k + k_{\rm on}R_0^3\left(\tilde{\zeta}k_{\rm on}c_0 + 2D_bk_{\rm off}\tilde{\eta}\right) = 0 \tag{S.32}$$

When binding is omitted $(k_{\text{off}} = 0)$ this reduces to a simple monotonic relation in the activity:

$$k_{\text{max},0} = -\tilde{\zeta} \frac{c_0 R_0}{4D\tilde{\eta}} \tag{S.33}$$

Appendix B: Free Energy Cost of Perturbing Defect Position.

For the polarisation field around the perturbed defect we have the expression:

$$\boldsymbol{p}_{l=1} = \boldsymbol{e}_r - \delta z \frac{R_0 - r}{r(R_0 - R_{c0})} \left(\partial_{\theta} Y_1^0 \boldsymbol{e}_{\theta} + \frac{1}{\sin(\theta)} \partial_{\phi} Y_1^0 \boldsymbol{e}_{\phi} \right).$$

Integrating the bulk free energy we find that the increase in free energy from such a perturbation is

$$\Delta F \approx \frac{\delta z^2 K}{R_{c0} (1 - \epsilon)^2} \left[1 - \epsilon^2 - 2\epsilon \log \left(\epsilon \right) \right]$$

where $\epsilon = R_{c0}/R_0$. Note that the value of this energy change is highly sensitive to the parameter R_{c0} which is physically difficult to define. This is because it is an approximation to the polar to isotropic phase transition that occurs near to the defect, which can be numerically simulated by a Landau De-Gennes type free energy, but the radial not analytically tractable.

Appendix C: Strong Anchoring Approximation for Active Polar Drop.

A general perturbation to the polarisation field that preserves |p|=1 can be written in spherical coordinates as:

$$\boldsymbol{p} = \hat{\boldsymbol{r}} + \sum_{l=2}^{\infty} \sum_{m=-l}^{l} f_{lm}(r) \delta p_{lm}^{(1)}(t) \left(\frac{\partial Y_{l}^{m}}{\partial \theta} - \frac{1}{\sin(\theta)} \frac{\partial Y_{l}^{m}}{\partial \phi} \right) \hat{\boldsymbol{e}}_{\theta} + g_{lm}(r) \delta p_{lm}^{(2)}(t) \left(\frac{\partial Y_{l}^{m}}{\partial \theta} + \frac{1}{\sin(\theta)} \frac{\partial Y_{l}^{m}}{\partial \phi} \right) \hat{\boldsymbol{e}}_{\phi}.$$

In order to find a functional form for $f_{lm}(r)$ and $g_{lm}(r)$ one would need to calculate the resulting flows in terms of these functions, and solve the polarisation dynamics equations for these functions. We find that this is not an analytically tractable problem. Instead, we look for a suitable ansatz for the form of $f_{lm}(r)$ and $f_{lm}(r)$. First, we consider the limit of strong anchoring, this gives the boundary condition $\mathbf{p} = \hat{\mathbf{n}}$ at r = R, meaning (to linear order) $f_{lm}(R_0)\delta p_{lm}^{(1)}(t) = -\delta R_{lm}(t)/R_0$ and $g_{lm}(R_0)\delta p_{lm}^{(2)}(t) = 0$. Secondly, as discussed in the text, we consider the case where the polarisation in the bulk is strongly coupled to that at interface. An intuitive assumption may be to solve for $h_{\perp} = 0$ to first order, as we did for the l = 1 mode, but this yields a result with irrational powers of r. If we consider instead the polarisation field as rigid spokes, the deformation is described by $f_{lm}(R_0) = -\delta R_{lm}(t)/(R_0\delta p_{lm})$ and $g_{lm}(R_0) = 0$, in other words there is no r-dependence. We find that this assumption leads to physically sensible results for a wide parameter range and it results in simple to understand results which reflect qualitatively what is observed in simulations. The important outcome of this is that, as long at the perturbation to the polarisation is small (and does not go to infinity at the origin), regardless of our choice of the r dependence of the perturbation, we see that the active part of the flow always deforms the interface in the way. In other words contractile activity acts to promote the deformation, while extensile acts to reduce the deformation.

Using this perturbation (equation (7)) we can first calculate partial solutions for the velocity and pressure that balance the force terms in the Stokes equation $(\eta_0 \nabla^2 v + \nabla \cdot \sigma_{act} + \sigma_{dis})$, the partial solution for the velocity is:

$$\mathbf{v}_{\text{part}} = -\frac{\delta R_{lm}}{R_0 \eta_0} \left\{ \zeta \frac{l(l+1)r}{(l+3)(l-2)} + \frac{K}{2r} \left((1+\nu)l(l+1) - 2\nu \right) \right\} Y_l^m(\theta, \phi) \hat{\mathbf{e}}_r
-\frac{\delta R_{lm}}{R_0 \eta_0} \left\{ \zeta \frac{3r}{(l+3)(l-2)} + \frac{K}{2l(l+1)r} \left((1+\nu)l(l+1) - 2\nu \right) \right\} r \nabla Y_l^m(\theta, \phi)$$
(S.34)

Note that the active part of this flow solution appears to diverge for l=2, however if we specifically solve for l=2 we see that this is because the actual form of this is proportional to $r^2 \log(r)$ (the solution containing the term of this form is plotted in figure 4). However, using the general form above results in the same eventual result for the stability analysis. These partial solutions can then be added to the general solutions for flow around a sphere (equations (S.9), (S.10) and (S.11)) so that one can solve the flow and stress continuity boundary conditions at r=R:

$$\left. \boldsymbol{v}^{\text{ext}} \right|_{r=R} - \boldsymbol{v} \right|_{r=R} = 0 \tag{S.35}$$

$$\hat{\boldsymbol{n}} \cdot \left[\underline{\underline{\sigma}}_{\text{tot}} - 2\eta_1 \underline{\underline{u}}^{\text{ext}} \right] \Big|_{r=R} = \boldsymbol{F}_{lm} + (P - P^{\text{ext}}) \hat{\boldsymbol{n}} \Big|_{r=R}.$$
 (S.36)

Note that the internal stress at the interface is no longer just the viscous stress, it also contains $\sigma_{\rm act}$ and $\sigma_{\rm dis}$. Also, we assume a constant surface tension γ_0 , so \boldsymbol{F}_{lm} now is as defined in the text for the active interface but with c=0. Solving the above boundary conditions for $a_{lm}^{(i)}$ and $b_{lm}^{(i)}$ we can substitute the full velocity solution into the equation for \dot{R} and find the resulting stability parameter. Note that because we are assuming a polarisation \boldsymbol{p} that is fixed by the anchoring, it is the radius dynamics that can be used to determine the stability. The resulting stability parameter λ is:

$$\lambda = -\frac{K}{2R_0^2 \eta_{\text{eff}}^2} \left\{ l(l-1)(l+2)\nu \left[3\eta_1 + 8l(l+1)(l+2)\tilde{\eta} \right] + l(l+1) \left[2\eta_0 (l(2l(l(l+5)+5)-5)-5) + \eta_1 (l(4l(l(l+5)+5)-7)-4) \right] \right\} - \zeta \left\{ \frac{l(l+1)(\eta_0 (l-1)(l(4l+9)+3) + \eta_1 (l(l(4l+5)-3)-3))}{(l+3)(\eta_1 + 2\eta_0 (l^2-1) + 2\eta_1 l^2)(\eta_0 (2l(l+2)+3) + 2\eta_1 l(l+2))} \right\} - \gamma_0 \left\{ \frac{(l-1)l(l+1)(l+2)(2l+1)(\eta_0 + \eta_1)}{R_0 (\eta_1 + 2\eta_0 (l^2-1) + 2\eta_1 l^2)(\eta_0 (2l(l+2)+3) + 2\eta_1 l(l+2))} \right\}$$
(S.37)

where $\eta_{\text{eff}}^2 = (\eta_1 + 2\eta_0 (l^2 - 1) + 2\eta_1 l^2) (\eta_0 (2l(l+2) + 3) + 2\eta_1 l(l+2))$. Then, the resulting contractile active threshold is found by solving $\lambda = 0$ for ζ . The resulting dispersion relation is very complex in terms of l, and hence we are able

to do little analytically to quantify it. However, we find that for a large parameter range the active threshold tends to increase in magnitude with mode number l, as one would expect. However, the distortion contribution (proportional to K) to the flow field in some instances ($\nu < -1$) appears to destabilise the drop at very large l. This is likely due to the assumption we make about the form of the polarisation perturbation, however the results appear to hold well for the l=2 mode, which we observe in the simulations as a symmetric deformation of the droplet.

In order to find this in 2D we work through exactly the same set of operations in polar coordinates, except that we assume that the polarisation scales as $p_{\theta} \propto r$, as using r^0 results in unphysical active flows. The resulting activity threshold is plotted in figure 5 for the simulation parameters using the k=2 mode.